Terahertz quantum-cascade-laser source based on intracavity difference-frequency generation

MIKHAIL A. BELKIN[1]*, FEDERICO CAPASSO[1], ALEXEY BELYANIN[2], DEBORAH L. SIVCO[3], ALFRED Y. CHO[3], DOUGLAS C. OAKLEY[4], CHRISTOPHER J. VINEIS[4] AND GEORGE W. TURNER[4]

[1]Harvard School of Engineering and Applied Sciences, Harvard University, Cambridge, Massachusetts 02138, USA
[2]Department of Physics, Texas A&M University, College Station, Texas 77843, USA
[3]Bell Laboratories, Lucent Technologies, Murray Hill, New Jersey 07974, USA
[4]Lincoln Laboratory, Massachusetts Institute of Technology, Lexington, Massachusetts 02420, USA
*e-mail: mbelkin@seas.harvard.edu

Published online: 1 May 2007; doi:10.1038/nphoton.2007.70

The terahertz spectral range ($\lambda = 30-300\,\mu$m) has long been devoid of compact, electrically pumped, room-temperature semiconductor sources[1–4]. Despite recent progress with terahertz quantum cascade lasers[2–4], existing devices still require cryogenic cooling. An alternative way to produce terahertz radiation is frequency down-conversion in a nonlinear optical crystal using infrared or visible pump lasers[5–7]. This approach offers broad spectral tunability and does work at room temperature; however, it requires powerful laser pumps and a more complicated optical set-up, resulting in bulky and unwieldy sources. Here we demonstrate a monolithically integrated device designed to combine the advantages of electrically pumped semiconductor lasers and nonlinear optical sources. Our device is a dual-wavelength quantum cascade laser[8] with the active region engineered to possess giant second-order nonlinear susceptibility associated with intersubband transitions in coupled quantum wells. The laser operates at $\lambda_1 = 7.6\,\mu$m and $\lambda_2 = 8.7\,\mu$m, and produces terahertz output at $\lambda = 60\,\mu$m through intracavity difference-frequency generation.

As mid-infrared quantum cascade lasers (QCLs) have been shown to operate continuous-wave (c.w.) above 400 K (ref. 9), we believe that this approach can eventually lead to a room-temperature, electrically pumped c.w. semiconductor terahertz (THz) source.

Difference-frequency generation (DFG) is a nonlinear optical process in which two beams at frequencies ω_1 and ω_2 interact in a medium with second-order nonlinear susceptibility, $\chi^{(2)}$, to produce radiation at frequency $\omega = \omega_1 - \omega_2$. The intensity of the wave at frequency $\omega = \omega_1 - \omega_2$ is given by the expression

$$W(\omega = \omega_1 - \omega_2) = \frac{\omega^2}{8\varepsilon_0 c^3 n(\omega_1) n(\omega_2) n(\omega)} |\chi^{(2)}|^2 \times \frac{W(\omega_1) W(\omega_2)}{S_{\text{eff}}} \times l_{\text{coh}}^2 \qquad (1)$$

where $l_{\text{coh}} = (|\mathbf{k} - (\mathbf{k}_1 - \mathbf{k}_2)|^2 + (\alpha/2)^2)^{-1}$ is the coherence length, $W(\omega_i)$, $n(\omega_i)$, and $\mathbf{k}_i$ are the power, refractive index, and wave vector of the beam at frequency ω_i, respectively, α indicates the losses at the DFG frequency, S_{eff} is the effective area of interaction[5,10,11] (see also Supplementary Information, pages 1–4, for details of Eq. (1) derivation), and we assumed that the medium is transparent for both pumps and neglected the depletion of the pump powers in the DFG process[5]. The symbol ε_0 is the permittivity of free space and c is the speed of light in a vacuum. It follows from equation (1) that, for efficient DFG, one needs to use materials with large $\chi^{(2)}$, input beams of high intensity, and achieve low losses and phase matching, $|\mathbf{k} - (\mathbf{k}_1 - \mathbf{k}_2)| \approx 0$. Most of the schemes to generate THz radiation using DFG use focused beams from high-intensity, pulsed, solid-state lasers (usually $\sim 1\,\text{GW cm}^{-2}$, often limited by the damage threshold of the nonlinear crystal) and/or achieve a large coherence length of tens of millimetres by either true phase matching or quasi-phase matching in transparent nonlinear crystals[5–7]. For intracavity DFG in dual-wavelength semiconductor lasers, the intensities of the pump beams are limited to $1-10\,\text{MW cm}^{-2}$, and the coherence length is limited to hundreds of micrometres by free-carrier absorption at THz frequencies. It appears impossible to achieve efficient THz DFG in such devices[12–14], unless the nonlinear susceptibility is significantly enhanced.

Quantum-well structures with giant optical nonlinearities in the mid- and far-infrared can be engineered by tailoring optical transitions within the same band, known as intersubband transitions[15–19]. In particular, a coupled quantum-well structure with $\chi^{(2)} = 10^6\,\text{pm V}^{-1}$ for DFG at $60\,\mu$m, four orders of magnitude larger than that of traditional nonlinear crystals (such as $LiNbO_3$, GaP and GaAs)[5,11] has been reported in ref. 18. In principle, such $\chi^{(2)}$ would enable efficient THz generation even for relatively low pump intensities and coherence lengths. However, high optical nonlinearity in these structures is achieved because all interacting fields are in resonance with intersubband transitions. This results in strong absorption of the pump and THz-DFG beams and unavoidably limits THz-DFG efficiency. The problem can be solved by designing an active nonlinear semiconductor device with the coupled quantum-well states,

providing both laser gain and giant $\chi^{(2)}$. In this case, instead of resonant absorption of the pump frequency, one has laser gain, whereas intrawaveguide generation of all interacting fields provides their tightest possible confinement and overlap, as reported for second-harmonic generation in QCLs[20–22].

It is vital to have strong pump beams in order to have efficient DFG. Therefore, we have studied ways to incorporate a giant $\chi^{(2)}$ into QCL designs that are known to produce high output powers and to work at room temperature. We have realized that a 'bound-to-continuum' QCL design[23] intrinsically possesses strong optical nonlinearity for THz DFG and can be further optimized for each particular case. We have designed the QCL active region to be composed of two substacks. The first substack (Fig. 1a) contains 30 stages of a 'bound-to-continuum' structure with laser emission wavelength of 8.9 μm and giant $\chi^{(2)}$ for THz DFG. The second substack (Fig. 1b) contains 20 stages of a 'two-phonon resonance' QCL structure[23] with a laser-emission wavelength of 7.9 μm and a relatively small $\chi^{(2)}$ for DFG.

A schematic of the THz-DFG process in our device is presented in Fig. 1c, with the relevant energy levels shown in bold and labelled in Fig. 1a. For a resonant DFG process, the expression for the nonlinear susceptibility[5,10,11] simplifies to

$$\chi^{(2)}(\omega=\omega_1-\omega_2)\approx N_e\frac{e^3}{\hbar^2\varepsilon_0}\sum_{n,n'}\frac{z_{1n}z_{nn'}z_{n'1}}{(\omega-\omega_{nn'}+i\Gamma_{nn'})}\times\left(\frac{1}{(\omega_1+\omega_{n'1}+i\Gamma_{n'1})}+\frac{1}{(-\omega_2-\omega_{n1}+i\Gamma_{n1})}\right) \quad (2)$$

where N_e is the electron density in the upper laser level 1, n and n' are the levels in the dense manifold of states (Fig. 1a), z_{ij}, ω_{ij} and Γ_{ij} are the dipole-matrix element, frequency and broadening of the transition between states i and j. e is the electron charge and h is the reduced Planck's constant. Here we assumed that most of the electron population is in the upper laser level 1 and neglected the populations in the lower laser levels. We calculate that by far the largest contribution to $\chi^{(2)}$ comes from states 1, 3 and 4 in Fig. 1a and c. Inserting the calculated dipole-matrix elements and energy spacings into equation (2), and assuming broadenings $\Gamma_{ij}\approx 10$ meV, and that most of the electrons are in the upper laser state 1, we obtain $\chi^{(2)}\approx 4\times10^5\,\mathrm{pm\,V^{-1}}$ for a DFG process between two laser pumps. We note that the real value of $\chi^{(2)}$ is certainly smaller because of the more uniform electron population distribution in the laser states. There is also uncertainty in the values of the intersubband transition energies and linewidths.

Our devices are based on InGaAs/AlInAs heterostructures, grown by molecular beam epitaxy (MBE) and lattice-matched to the InP substrate. We used a 10-μm-thick InP top waveguide cladding, grown by metallorganic chemical vapour deposition (MOCVD), to provide dielectric mode confinement for the mid-infrared and THz modes (Fig. 2).

A typical mid-infrared emission spectrum from ridge-waveguide devices is shown in the inset of Fig. 3 along with typical current versus voltage, I–V, and light output versus current, L–I, characteristics. The devices operated in dual-wavelength mode up to 250 K and still provided single-wavelength emission ($\lambda\approx7.6$ μm) at room temperature.

Terahertz spectra from a representative device are shown in Fig. 4a. The spectral position of the THz signal is in agreement with the difference in the frequencies of the mid-infrared pumps. The maximum DFG output power at 10 K and 80 K was comparable, and it was approximately a factor of 5 smaller at 150 K, the maximum temperature at which DFG was observed.

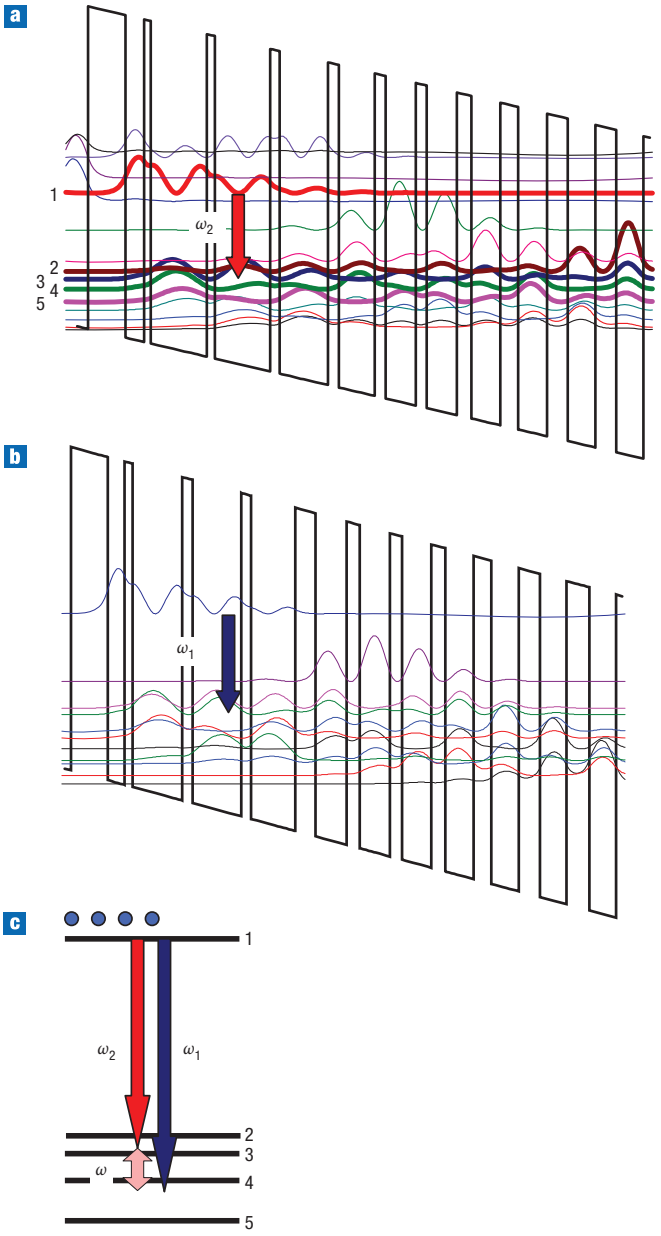

Figure 1 Band-structure design and THz-DFG process. a,**b**, Calculated conduction-band diagrams of one period of (**a**) the 30-stage stack of a 'bound-to-continuum' quantum-cascade-laser design with integrated second-order optical nonlinearity and (**b**) the 20-stage stack of a 'two-phonon resonance' quantum-cascade-laser design. The wavy curves represent the moduli squared of the wavefunctions of the relevant quantum states. The electron states in the 'bound-to-continuum' section important for difference-frequency generation are shown in bold and labelled 1 to 5 (**a**). The layer sequences for the two designs (in Å), starting from the injector barrier, are **40**, 20, **7**, 60, **9**, 59, **10**, 52, **12**, 38, **12**, 32, **12**, 32, **16**, 31, **19**, 31, **22**, 30, **22**, 29 and **40**, 18, **9**, 54, **11**, 53, **11**, 48, **22**, 34, **14**, 33, **13**, 32, **15**, 31, **19**, 30, **23**, 29, **25**, 29, respectively. The barriers are indicated in bold face and the underlined layers are doped to $n=4\times10^{17}\,\mathrm{cm^{-3}}$. **c**, Diagram showing the difference-frequency generation process between the electron states in the 'bound-to-continuum' section.

The decrease with temperature of the DFG signal can be attributed to the reduction of the mid-infrared pump powers with temperature. In particular, the product of the peak powers

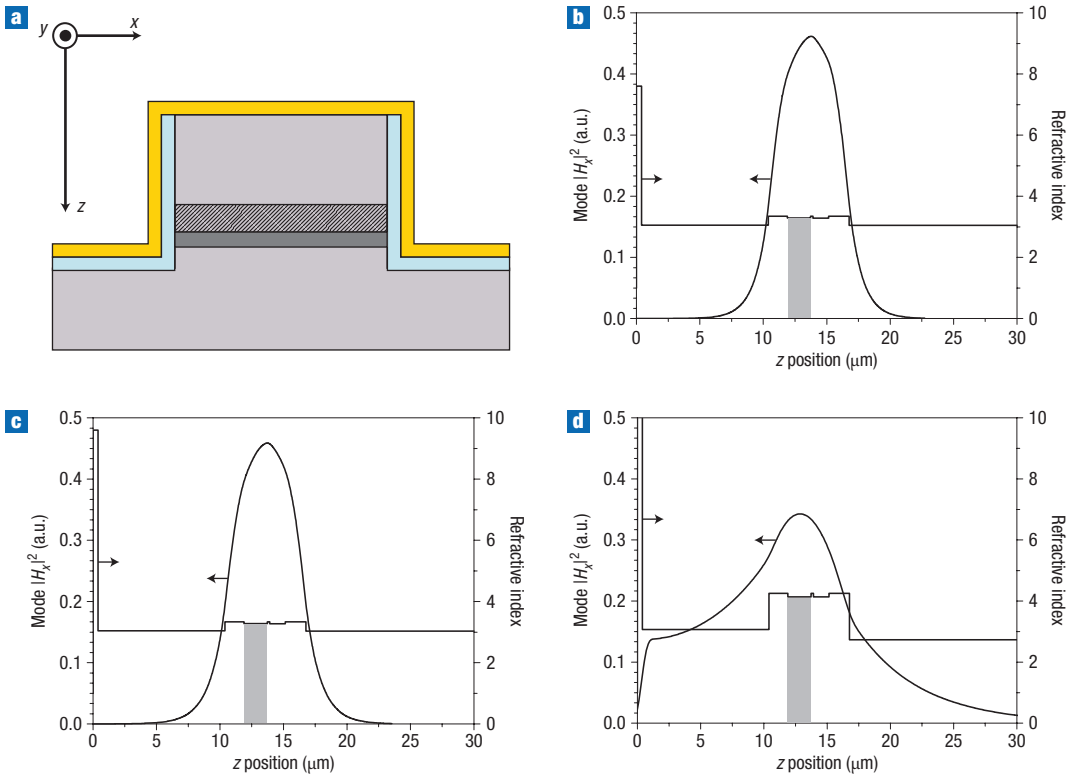

Figure 2 Waveguide design and the laser modes. a, Schematic of the waveguide structure, showing the gold layer in yellow, the Si_3N_4 layer in blue, and the semiconductor in grey. The two sections of the QCL active region are shown in dark grey. The section with the large nonlinear susceptibility is shaded. **b–d**, The magnetic-field intensity H_x in the TM_{00} waveguide mode for wavelengths at $\lambda = 7.6\,\mu m$ (**b**), 8.7 μm (**c**) and 60 μm (**d**). The values of H_x are normalized so that $\int (H_x)^2\,dz = 1$, where the z coordinate is expressed in micrometres. Also shown is the refractive-index profile, with the region with large nonlinear susceptibility shaded. For the TM_{00} modes in a 20-μm-wide ridge waveguide, we obtain effective-refractive-index values (n_{eff}) of $3.266 + i \times 0.00057$, $3.248 + i \times 0.00080$, and $2.981 + i \times 0.161$ for the wavelengths 7.6 μm, 8.7 μm and 60 μm, respectively.

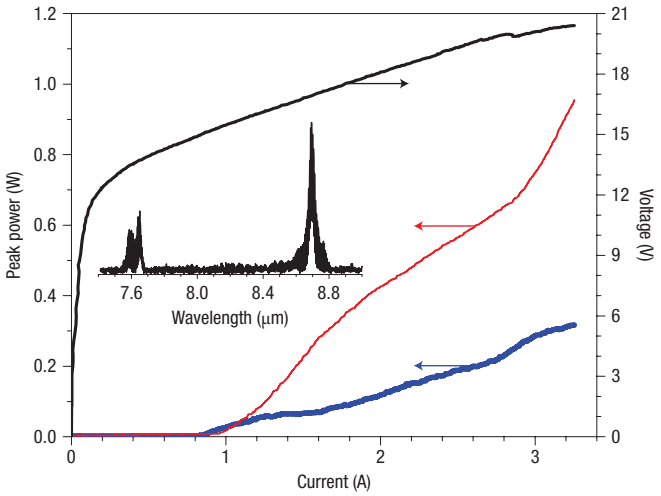

Figure 3 Light output versus current (*L–I*), red and blue lines, and current versus voltage (*I–V*), black line, characteristics obtained at 10 K in pulsed mode (60-ns pulses at 200 kHz) with a 20-μm-wide, 2-mm-long ridge device with a high-reflection coating on a back facet. The peak powers of the 7.6-μm and 8.7-μm pump lasers are plotted as thick blue and thin red lines, respectively. The data are not corrected for the estimated 70% power collection efficiency. The inset shows the mid-infrared spectrum of the device operated in pulsed mode at high currents.

of the two mid-infrared pumps at 10 K and 80 K was similar and that at 150 K was smaller by approximately a factor of 4. The dependence of the peak THz-DFG power and of the total mid-infrared emission power on the injection current at 10 K for a typical device is shown in Fig. 4b. The THz-DFG power versus the product of the powers of two mid-infrared pumps is plotted in the inset of Fig. 4b. A linear dependence, expected from equation (1), is clearly observable, with a slope efficiency of $11\,nW\,W^{-2}$. As an additional proof that the observed THz signal is DFG and not laser luminescence, in Fig. 5a,b we demonstrate a correlation between the mid-infrared emission and the THz-DFG spectra for two ridge lasers that had slightly different mid-infrared emissions.

In these first proof-of-principle THz-DFG devices, we did not attempt to achieve phase matching. We estimate the phase mismatch between the gaussian-transverse-magnetic-beam, TM_{00}, pump and THz-DFG modes, $\mathbf{k} - (\mathbf{k}_1 - \mathbf{k}_2)$, to be approximately $420\,cm^{-1}$ and the losses for THz-DFG (α) to be $\sim 340\,cm^{-1}$, which translates into a coherence length of $\sim 22\,\mu m$ (see equation (1)). Theoretical estimates using $l_{coh} = 22\,\mu m$, $\chi^{(2)} \approx 4 \times 10^5\,pm\,V^{-1}$, and assuming mid-infrared lasing only in TM_{00} modes, predict DFG conversion efficiency to be of the order of $1\,mW\,W^{-2}$ in a waveguide geometry (see Supplementary Information, pages 3–4, for details of the calculation). The measured value of the conversion efficiency, corrected for the mid-infrared and THz-DFG signal-collection efficiencies (see Methods), is approximately $50\,nW\,W^{-2}$. The discrepancy may

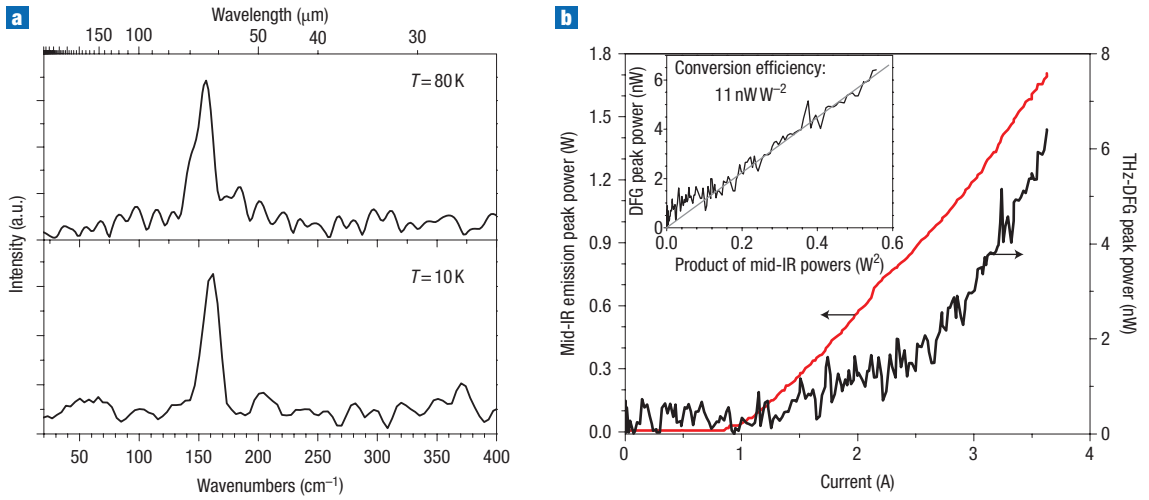

Figure 4 Spectral characteristics and power dependence of THz DFG. a, Terahertz DFG spectra obtained at different temperatures from a 20-μm-wide, 2-mm-long ridge device with a high-reflection coating on a back facet. The device was operated in pulsed mode with peak current of 3.6 A in 60-ns pulses at 500 kHz. **b**, *L*–*I* plots for THz-DFG power (black line and right axis) and mid-infrared (mid-IR) emission power (red line and left axis) obtained at 10 K in pulsed mode (60-ns pulses at 500 kHz) with a 20-μm-wide, 2-mm-long ridge device with a back facet, high-reflection coating. The inset shows the THz-DFG signal intensity plotted versus the product of the two mid-infrared pump powers (black line) and a linear fit (grey line). The data are not corrected for the estimated 70% and <10% power collection efficiencies for mid-infrared and THz measurements, respectively.

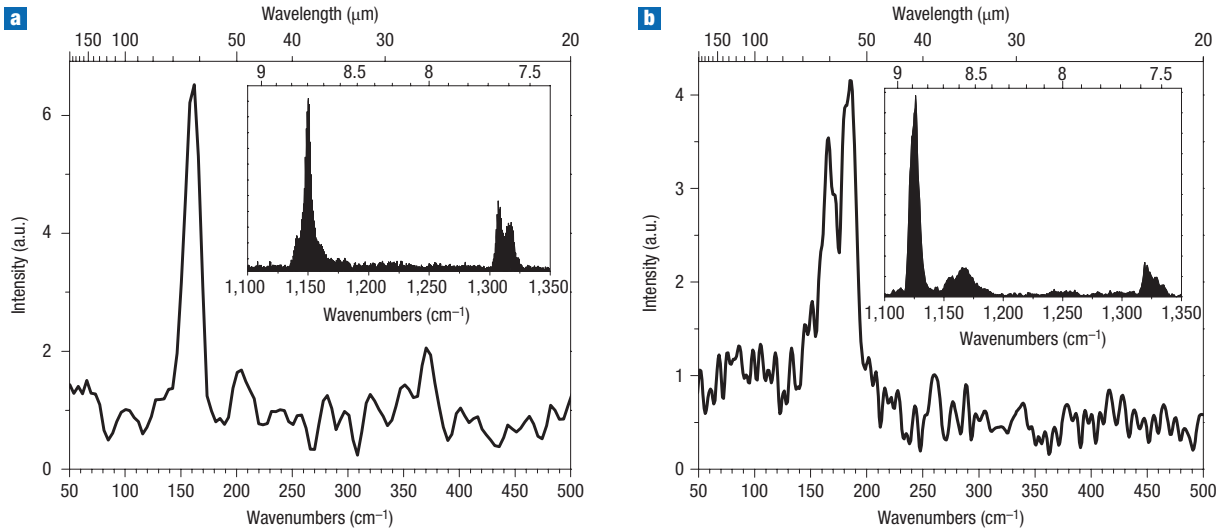

Figure 5 Dependence of THz-DFG spectra on mid-infrared emission spectra (inset). a,**b**, Results for two different 20-μm-wide, 2-mm-long ridge devices with a high-reflection coating on a back facet. The devices were operated at 10 K in pulsed mode with 60-ns pulses at 500 kHz; the injection current was set at 3.6 A. The peak position in the THz-DFG emission spectrum in Fig. 4a agrees with the frequency spacing between the peaks in the mid-infrared emission spectrum. In Fig. 4b, the frequency spacings between the high-frequency peak and the two low-frequency peaks in the mid-infrared emission spectrum are 155 and 195 cm^{-1}. This results in the THz-DFG emission spectrum displaying two peaks, centred at 165 and 185 cm^{-1}. The positions of the peaks in the THz-DFG spectrum are shifted towards one another due to their superposition and to the frequency dependence of $\chi^{(2)}$.

result from a number of factors, including mid-infrared lasing in many higher order lateral modes, the actual value of $\chi^{(2)}$ being significantly smaller, poor THz-wave outcoupling[24,25], and so on. A good understanding of the mechanisms leading to this discrepancy is important for designing efficient THz-DFG QCLs.

In conclusion, we have demonstrated a new compact semiconductor THz source based on DFG in QCLs. We have generated approximately 60 nW of THz power, corrected for the collection efficiency, at $T = 80$ K. Work is now under way to understand the factors reducing THz-DFG efficiency from the theoretical estimate and to improve the efficiency of THz DFG by achieving phase matching, using surface-emission schemes, and improving the design of the active region and heterostructure growth quality. In particular, we anticipate that, with proper waveguide design, the coherence length may be increased to ~100 μm or more and S_{eff} may be decreased by

50% or more, which would result in a factor of ~30 or more increase in THz DFG power; see equation (1). Our preliminary calculations also show that the surface-emission scheme using a second-order grating for THz DFG may improve the DFG outcoupling efficiency by a factor of 10 or more, while the waveguide properties for the mid-infrared pumps remain virtually unchanged. Improvements in the design of the active region and growth quality may lead to further significant improvements in THz-DFG output power. Overall, although significant work still needs to be carried out to fully optimize THz DFG in QCLs, based on the results reported here, microwatt-power c.w. intracavity THz DFG should be within reach for QCLs operating at thermoelectrically cooler temperatures. Further optimization may eventually lead to THz-DFG QCLs providing up to milliwatts of THz power at room temperature.

METHODS

DEVICE

The MBE growth started on an InP substrate, n-doped to $n = 1.3–1.8 \times 10^{17}\,\mathrm{cm}^{-3}$, with a 1.6-μm-thick GaInAs layer, n-doped to $n = 5 \times 10^{16}\,\mathrm{cm}^{-3}$, acting as lower waveguide core, on top of which 20 stages of the 'double-phonon resonance' active region and 30 stages of the 'bound-to-continuum' active region were grown, separated by a 200-nm-thick GaInAs spacer, n-doped to $n = 5 \times 10^{16}\,\mathrm{cm}^{-3}$. The growth ended with a 1.5-μm-thick GaInAs layer, n-doped to $n = 5 \times 10^{16}\,\mathrm{cm}^{-3}$, acting as upper waveguide cladding. The wafer was then transferred to an MOCVD chamber and a 10-μm-thick InP layer, n-doped to $n = 1 \times 10^{17}\,\mathrm{cm}^{-3}$, was overgrown to provide the top waveguide cladding for both mid-infrared and THz modes.

The material was processed into deep-etched ridge waveguides 2 mm long and 15–25 μm wide, with a 400-nm-thick Si_3N_4 insulating layer on the lateral walls of the ridge and a Ti/Au (20 nm/400 nm) top contact (Fig. 2a). A non-alloyed Ge/Au contact was deposited on the back. A high-reflectivity coating, consisting of Al_2O_3/Au (200 nm/50 nm) layers was evaporated on the back facet of the devices. The samples were indium-soldered on Ni/Au plated copper holders and mounted in a liquid-helium flow cryostat.

MEASUREMENTS

A Fourier-transform infrared spectrometer was used for spectral measurements of both the mid-infrared and the THz emission. A mercury cadmium telluride detector and a helium-cooled silicon bolometer were used for mid-infrared and THz spectral measurements, respectively. Power measurements were carried out with a calibrated thermopile detector and a calibrated bolometer for mid-infrared and THz emission, respectively. We estimate the power collection efficiency to be approximately 70% for mid-infrared and <10% for THz measurements. The data presented in the figures are not corrected for the collection efficiency. Optical filters were used in order to discriminate both mid-infrared pumps and THz DFG.

Received 1 February 2007; accepted 20 March 2007; published 1 May 2007.

References

1. Brundermann, E. *et al.* High duty cycle and continuous terahertz emission from germanium. *Appl. Phys. Lett.* **76,** 2991–2993 (2000).
2. Köhler, R. *et al.* Terahertz semiconductor-heterostructure laser. *Nature* **417,** 156–159 (2002).
3. Rochat, M. *et al.* Low-threshold terahertz quantum-cascade lasers. *Appl. Phys. Lett.* **81,** 1381–1383 (2002).
4. Williams, B. S. *et al.* Operation of terahertz quantum-cascade lasers at 164 K in pulsed mode and at 117 K in continuous-wave mode. *Opt. Express* **13,** 3331–3339 (2005).
5. Shen, Y. R. *The Principles of Nonlinear Optics* (John Wiley & Sons, New York, 1984).
6. Tanabe, T. *et al.* Frequency-tunable terahertz wave generation via excitation of phonon-polaritons in GaP. *J. Phys. D* **36,** 953–957 (2003).
7. Vodopyanov, K. L. *et al.* Terahertz-wave generation in quasi-phase-matched GaAs. *Appl. Phys. Lett.* **89,** 141119 (2006).
8. Faist, J. *et al.* Quantum cascade laser. *Science* **264,** 553–556 (1994).
9. Diehl, L. *et al.* High-power quantum cascade lasers grown by low-pressure metal organic vapor-phase epitaxy operating in continuous wave above 400 K. *Appl. Phys. Lett.* **88,** 201115 (2006).
10. Butcher, P. N. & Cotter, D. *The Elements of Nonlinear Optics* (Cambridge Univ. Press, Cambridge, 1990).
11. Boyd, R. W. *Nonlinear Optics* (Academic Press, New York, 2003).
12. Hoffmann, S. *et al.* Four-wave mixing and direct terahertz emission with two-color semiconductor lasers. *Appl. Phys. Lett.* **84,** 3585–3587 (2004).
13. Hoffmann, S. *et al.* Two-colour diode lasers for generation of THz radiation. *Semicond. Sci. Technol.* **20,** S205–S210 (2005).
14. Hoffmann, S. *et al.* Bandwidth limitations of two-colour diode lasers for direct terahertz emission. *Electron. Lett.* **42,** 696–697 (2006).
15. Fejer, M. M. *et al.* Observation of extremely large quadratic susceptibility at 9.6–10.8 μm in electric field biased AlGaAs/GaAs quantum wells. *Phys. Rev. Lett.* **62,** 1041–1044 (1989).
16. Capasso, F. *et al.* Coupled quantum well semiconductors with giant electric field tunable nonlinear optical properties in the infrared. *IEEE J. Quant. Electron.* **30,** 1313–1326 (1994).
17. Rosencher, E. *et al.* Quantum engineering of optical nonlinearities. *Science* **271,** 168–173 (1996).
18. Sirtori, C. *et al.* Far-infrared generation by doubly resonant difference frequency mixing in a coupled quantum well two-dimensional electron gas system. *Appl. Phys. Lett.* **65,** 445–447 (1994).
19. Dupont, E. *et al.* Terahertz emission in asymmetric quantum wells by frequency mixing of midinfrared waves. *IEEE J. Quant. Electron.* **42,** 1157–1174 (2006).
20. Owschimikow, N. *et al.* Resonant second-order nonlinear optical processes in quantum cascade lasers. *Phys. Rev. Lett.* **90,** 043902 (2003).
21. Gmachl, C. *et al.* Optimized second-harmonic generation in quantum cascade lasers. *IEEE J. Quant. Electron.* **39,** 1345–1355 (2003).
22. Malis, O. *et al.* Milliwatt second harmonic generation in quantum cascade lasers with modal phase matching. *Electron. Lett.* **40,** 1586–1587 (2004).
23. Faist, J. *et al.* Bound-to-continuum and two-phonon resonance quantum-cascade lasers for high duty cycle, high-temperature operation. *IEEE J. Quant. Electron.* **38,** 533–546 (2002).
24. Kohen, S. *et al.* Electromagnetic modeling of terahertz quantum cascade laser waveguides and resonators. *J. Appl. Phys.* **97,** 053106 (2005).
25. Fan, J. A. *et al.* Surface emitting terahertz quantum cascade laser with a double-metal waveguide. *Opt. Express* **14,** 11672–11680 (2006).

Acknowledgements

This work was supported by Air Force Office of Scientific Research under Contract No. FA9550-05-1-0435. A.B. acknowledges partial support from National Science Foundation through grants ECS-0547019, EEC-0540832 and OISE 0530220. Fabrication was carried out in the Center for Nanoscale Systems at Harvard University. Harvard-CNS is a member of the National Nanotechnology Infrastructure Network.

Correspondence and requests for materials should be addressed to M.A.B. or F.C.

Supplementary information accompanies this paper on www.nature.com/naturephotonics.

Competing financial interests

The authors declare no competing financial interests.